PHYSICAL REVIEW FLUIDS **2**, 093601 (2017)

Shock waves from nonspherical cavitation bubbles

Outi Supponen,[1,*] Danail Obreschkow,[2] Philippe Kobel,[1] Marc Tinguely,[1]
Nicolas Dorsaz,[1] and Mohamed Farhat[1]

[1]*Laboratory for Hydraulic Machines, Ecole Polytechnique Fédérale de Lausanne,*
Avenue de Cour 33bis, 1007 Lausanne, Switzerland

[2]*International Centre for Radio Astronomy Research, University of Western Australia,*
7 Fairway, Crawley, Western Australia 6009, Australia

(Received 27 February 2017; published 1 September 2017)

We present detailed observations of the shock waves emitted at the collapse of single cavitation bubbles using simultaneous time-resolved shadowgraphy and hydrophone pressure measurements. The geometry of the bubbles is systematically varied from spherical to very nonspherical by decreasing their distance to a free or rigid surface or by modulating the gravity-induced pressure gradient aboard parabolic flights. The nonspherical collapse produces multiple shocks that are clearly associated with different processes, such as the jet impact and the individual collapses of the distinct bubble segments. For bubbles collapsing near a free surface, the energy and timing of each shock are measured separately as a function of the anisotropy parameter ζ, which represents the dimensionless equivalent of the Kelvin impulse. For a given source of bubble deformation (free surface, rigid surface, or gravity), the normalized shock energy depends only on ζ, irrespective of the bubble radius R_0 and driving pressure Δp. Based on this finding, we develop a predictive framework for the peak pressure and energy of shock waves from nonspherical bubble collapses. Combining statistical analysis of the experimental data with theoretical derivations, we find that the shock peak pressures can be estimated as jet impact-induced hammer pressures, expressed as $p_h = 0.45(\rho c^2 \Delta p)^{1/2}\zeta^{-1}$ at $\zeta > 10^{-3}$. The same approach is found to explain the shock energy decreasing as a function of $\zeta^{-2/3}$.

DOI: 10.1103/PhysRevFluids.2.093601

I. INTRODUCTION

Shock waves are one of the most destructive phenomena occurring during the collapse of cavitation bubbles and therefore a topic of long-standing interest. The associated pressures, reaching values on the order of GPa [1,2], are able to wear metallic surfaces, which is a classic concern for ship propellers and hydraulic turbines [3–5]. Further victims of cavitation-induced damage are, for example, artificial heart valves [6], liquid-propelled rocket engines [7], and the prey of a mantis shrimp [8]. The damaging power can also be exploited for beneficial uses such as in medical [9] (e.g., shock wave lithotripsy [10,11] and cancer therapy [9,12]) and cleaning [13] applications. However, predictive tools to characterize the key properties of cavitation-driven shocks are limited. In the quest of mitigating the harm they may cause or maximizing their benefit, we here make detailed observations of shocks of single cavitation bubbles and propose a framework to predict their strengths.

Much progress has been made in the prediction of the damage potential of shock waves emitted by spherically collapsing bubbles [2,14–17]. However, doing so for nonspherically collapsing bubbles is still an open problem. Bubbles may deform under the effect of, for example, nearby surfaces, inertial forces such as gravity, or passing shock waves. The collapse shock wave strengths have been shown, both experimentally and numerically, to vary with the bubble sphericity for bubbles collapsing near a rigid wall [18–21]. Shocks from bubbles collapsing under the effect of a passing shock wave have been shown to be sensitive to the latter's timing and strength [22]. The shocks emitted at the collapse

---

[*] outi.supponen@epfl.ch

of an individual bubble are often referred to as a single event, yet it is known that deformed bubbles that are pierced by high-speed microjets produce several shock waves from multiple locations upon collapse [19,23,24]. However, understanding the contribution of each shock emission mechanism to the final damage characteristics and a systematic study on the influence of the bubble deformation on them are still lacking, as recently pointed out by Lauterborn and Vogel [25]. Although numerical simulations offer an excellent means to reproduce complex shock wave scenarios associated with nonspherical collapses [26–29], observations for their validation are limited. Furthermore, we still lack an understanding of how the shocks from bubbles deformed by distinct sources differ.

In this work, shock wave energies and pressures are systematically measured as a function of the various bubble parameters and asymmetries. The objective is to understand how the deformation of bubbles affects their detailed collapse shock wave emission. In particular, we aim to estimate, through visualizations and pressure measurements, the strengths and the timings of the distinct shock waves produced at the collapse of bubbles with geometries varying from highly spherical to strongly deformed by a nearby free surface. These data are then compared to bubbles deformed by a nearby rigid surface and by the hydrostatic pressure gradient, which is modulated in variable gravity aboard parabolic flights (60th and 62nd European Space Agency parabolic flight campaigns and the first Swiss parabolic flight). The advantage of a gravity-induced pressure gradient to deform bubbles is its uniformity in time and space that leads to similar bubble collapse shapes across a wide range of bubble asymmetries [30]. Furthermore, any smooth pressure field can be approximated to first order by such a uniform pressure gradient. We exploit the large number of data and a broad parameter space to reach an empirical model for predicting the shock strengths for nonspherical bubbles, which is backed up by theoretical arguments. This model applies the scaling laws for microjets, which we have recently developed in detail [30], to the shock wave emission of deformed cavitation bubbles.

The deformation of bubbles collapsing near surfaces is usually quantified by the standoff parameter $\gamma = h/R_0$, where h is the distance between the bubble center and the surface and R_0 is the maximum bubble radius. Deformations caused by near surfaces and gravity can be compared by using the vector parameter $\boldsymbol{\zeta}$ [30,31]:

$$\boldsymbol{\zeta} = \begin{cases} -\rho \mathbf{g} R_0 \Delta p^{-1} & \text{(gravitational field)} \\ +0.195\gamma^{-2}\mathbf{n} & \text{(flat free surface)} \\ -0.195\gamma^{-2}\mathbf{n} & \text{(flat rigid surface),} \end{cases} \tag{1}$$

where ρ is the liquid density, $\mathbf{g}$ is the gravitational acceleration, $\Delta p = p_0 - p_v$ is the driving pressure (where p_0 is the static pressure of the unperturbed liquid at the location of the bubble and p_v is the vapor pressure), and $\mathbf{n}$ is the unit vector normal to the surface, in the direction from the surface to the bubble. Here $\boldsymbol{\zeta}$ is essentially the dimensionless equivalent of the Kelvin impulse, which is the linear momentum acquired by the liquid during the growth and the collapse of the bubble [32]. A higher $\zeta \equiv |\boldsymbol{\zeta}|$ causes a more pronounced bubble deformation and delineates key parameters of the microjet, such as the jet speed or the jet impact timing, almost irrespective of the source of deformation for $\zeta < 0.1$ [30]. We henceforth primarily use ζ to quantify bubble deformation, but also display the equivalent γ for convenience.

This paper is structured as follows. Section II presents the experimental methods, describing the setup and the relevant calibrations. Section III shows detailed observations of single and multiple shock waves emitted by bubbles near a free surface. A framework for predicting shock peak pressures and energies is then proposed in Sec. IV, along with comparisons between shocks from bubbles deformed by different sources (free and rigid surfaces and gravity). Finally, the results are discussed in Sec. V.

II. EXPERIMENTAL METHODS

The central components of our experimental setup are shown in Fig. 1. A pulsed laser is expanded and focused in demineralized water by an immersed parabolic mirror, which produces a pointlike

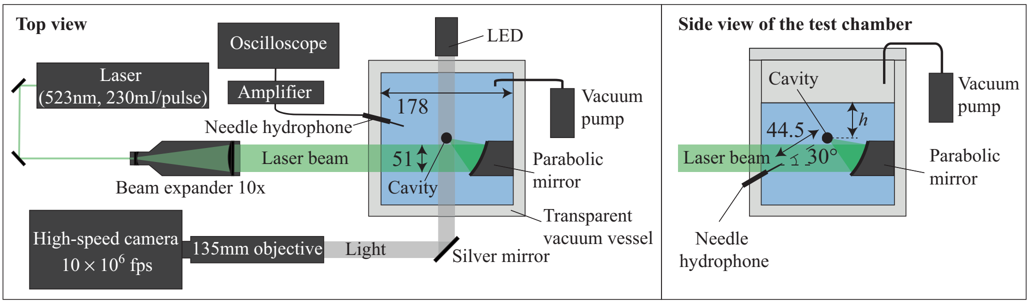

FIG. 1. Top and side view schematics of the experimental setup. The dimensions are given in mm.

plasma and thereby an initially highly spherical bubble [33] that grows and subsequently collapses. The bubble and the associated shock waves are visualized using shadowgraphy with an ultrahigh-speed camera (Shimadzu HPV-X2) reaching filming speeds up to 10×10^6 frames/s (fps) with a 50-ns exposure time and a collimated backlight beam from a light-emitting diode. The driving pressure Δp can be adjusted by varying the static pressure p_0 in the test chamber between 0.08 and 1 bar with a vacuum pump. Tuning the laser power generates bubbles of energies $E_0 = (4\pi/3)R_0^3\Delta p$ ranging from 0.1 to 28 mJ. This parameter space leads to a wide range of maximum bubble radii $R_0 = 1-10$ mm, which are large enough for viscosity and surface tension to have a negligible effect on the bubble dynamics [34].

To modulate the bubble deformation, we vary the bubble's distance to a surface ($h \sim 3-30$ mm) and/or the perceived gravity ($|\mathbf{g}| \sim 0-2\,g$, where $g = 9.81$ ms^{-2}), in addition to varying R_0 and Δp. The maximum radii are obtained from the recorded collapse time T_c (i.e., half oscillation time) of the bubble as $R_0 = 1.093T_c(\Delta p/\rho)^{1/2}\kappa^{-1}$ [35], where κ is a factor depending on the source and level of deformation. For bubbles collapsing near a free surface, κ is a lifetime-shortening factor that can be approximated as $\kappa \approx 1 - 0.102\gamma^{-1}$ [36]. The bubbles deformed by gravity or a nearby rigid surface in this work are at $\zeta < 10^{-2}$ and therefore the deformations are weak enough for them to justify the assumption $\kappa \approx 1$. All measurements are made at room temperature. Additional details on our experimental setup and the parabolic flights may be found in Ref. [33].

A needle hydrophone (75 μm sensor, manufactured by Precision Acoustics) is used to record the pressure of the shock waves. The bandwidth of this hydrophone is guaranteed to extend above 30 MHz and is thus capable of a detailed sampling of the shock waveform and of disentangling multiple fronts. The rise time upper bound is found to be approximately 15 ns, estimated from the time it takes for the pressure signal of the steep shock wave produced at the explosive bubble generation (Fig. 2) to rise from 10% to 90% of its maximum amplitude. The actual rise time of the

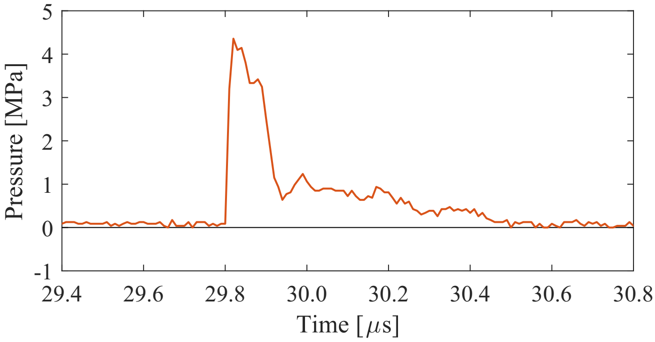

FIG. 2. Typical hydrophone pressure signal of the shock wave emitted at the bubble generation. Here $t = 0$ μs corresponds to the time instant of bubble generation.

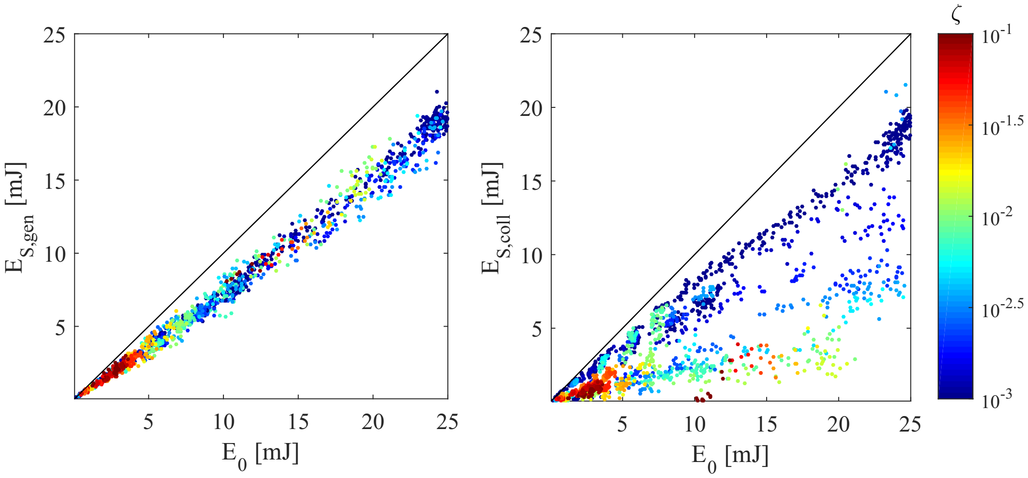

FIG. 3. Energies of shock waves emitted at bubble generation (left) and collapse (right) for various bubble energies E_0. The colors indicate the level of ζ. The solid lines show $E_S = E_0$.

shock wave is likely to be even shorter [37]. The pressure signal, represented by an electrical voltage, is amplified and recorded at a 100-MHz sampling frequency by an oscilloscope. The hydrophone sensor is located at a distance of $d = 44.5$ mm from the bubble center at an angle of 30° below the horizontal plane with a planar incidence of the shock wave onto the sensor. The shock waves take approximately 30 μs to reach the hydrophone after being generated. Being thin (needle thickness is 0.3 mm) and located far relative to the bubble size, the presence of the hydrophone needle is assumed to have a negligible effect on the bubble dynamics.

We assume spherical propagation of the shock waves and estimate their energies as

$$E_S = aU_{\max}^b \int U(t)^2 dt, \tag{2}$$

where $U(t)$ (V) is the hydrophone voltage signal (containing the full shock wave scenario in the case of multiple collapse shocks, but excluding any reflections from boundaries), $U_{\max}$ is the maximum value of $U(t)$, and a and b are calibration constants. If the shock propagated with no energy dissipation, then $a = 4\pi d^2(\rho c)^{-1}G^{-2}$ [18] (where c is the sound speed in the liquid and G is the gain in units of V/Pa) and $b = 0$. An exponent $b > 0$ is used to approximately compensate for nonlinear dissipation (e.g., due to inelastic heating, induced microcavitation, etc.), whose relative effect increases with pressure. As the precise gain G is unknown in our current setup and nonlinear dissipation is expected, we treat a and b as positive free parameters. We fit these parameters to simultaneously satisfy two conditions: (i) the energy of the laser-induced shock at the bubble generation $E_{S,\mathrm{gen}}$ scales linearly with the bubble energy E_0 [18] and (ii) the total energy of the shock(s) emitted at the bubble collapse $E_{S,\mathrm{coll}}$ is bounded by the difference between the bubble energy E_0 and the rebound energy E_{reb}. For bubbles that collapse spherically ($\zeta < 10^{-3}$) and produce no jets, we assume $E_{S,\mathrm{coll}} \approx E_0 - E_{\mathrm{reb}}$ [38]. We find that a is such that $E_{S,\mathrm{gen}}/E_0 \approx 0.75$ (i.e., 43% of the absorbed laser energy goes into the generation shock and 57% goes into the bubble) and $b \approx 0.45$, indicating slight nonlinear dissipation. Figure 3 displays the calibrated energies for both bubble generation and collapse shock waves for various E_0 and ζ, clearly showing the linear relationship between $E_{S,\mathrm{gen}}$ and E_0 and that the collapse shock energies tend to be lower for increasing ζ. Pressures are then computed from the calibrated energies as $p(t) = U(t)/G$, where the gain G is determined for each individual bubble separately as $G^2 = 4\pi d^2(\rho c)^{-1} \int U(t)^2 dt/E_S$. Using a variable G allows for the comparison of the signals obtained in different conditions, for which the recorded pressures are differently affected by the shock's nonlinear dissipation.

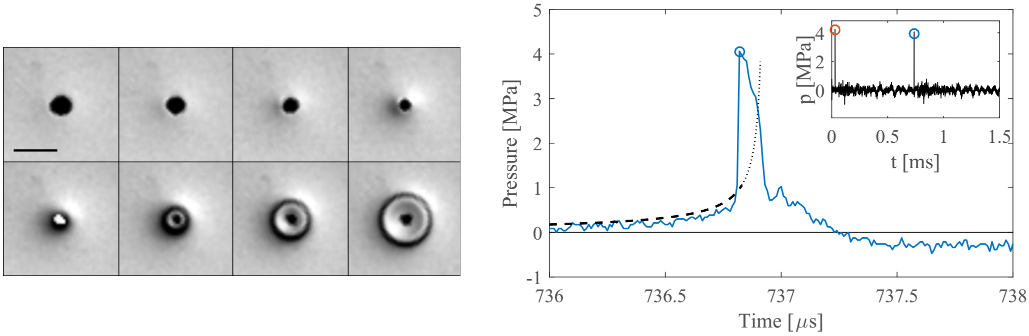

(a)

(b)

FIG. 4. Cavity of $R_0 = 3.8$ mm collapsing spherically at $\zeta < 10^{-3}$ and emitting a single shock wave. (a) High-speed shadowgraph visualization. The interframe time is 100 ns and the black bar shows the 1-mm scale. (See [39] for the corresponding movie.) (b) Pressure recorded by the hydrophone. The inset shows the whole bubble oscillation, where the orange and blue circles refer to generation and collapse shock wave peak pressures, respectively. The dashed line shows $p(t) - p_0$, where $p(t)$ is the Rayleigh pressure model computed from Eq. (3) up to the shock peak, and the dotted line extends the curve to the time at which the bubble is estimated to reach a radius of $R = 100$ μm.

III. DETAILED OBSERVATIONS

A. Spherical collapse

A spherical bubble collapse emits a single shock front that is spherically symmetrical, as visualized in Fig. 4(a). This shock is well studied and arises from the compression of the incondensable gases inside the bubble overcoming the high pressures in the liquid around the bubble in the final collapse stage, which makes the liquid rapidly invert its motion as the bubble rebounds [14]. The gases inside the bubble are compressed so violently that they heat up to temperatures reaching levels of visible light emission, a phenomenon known as luminescence, which is visible in frame 5 of Fig. 4(a) and implies that the bubble reaches its minimum size during the 50-ns exposure time of this image. The rebound bubble then forms a compression wave that propagates outward and quickly steepens to form a shock front, as can be seen in frames 6–8. The corresponding hydrophone measurement of the shock wave is shown in Fig. 4(b). Assuming $1/r$ spreading of the spherical wave and the luminescence spot in Fig. 4(a) as the minimum bubble size ($R_{\min} \approx 100$ μm), the lower bound for the peak pressure at the bubble wall at minimum bubble radius is estimated as 2 GPa, which is in agreement with previously estimated values [25]. The actual value is likely much higher, because we overestimate the minimum bubble radius that our apparatus is not able to capture due to the luminescence and the dark region around the bubble hiding this information. When using the Keller-Miksis model [40], where we adjust the initial gas pressure by numerically fitting the model to the observed radial evolution of the bubble (first and second oscillations), we would expect a minimum bubble radius of $R_{\min} \approx 15$ μm and thereby a peak pressure of 12 GPa.

In agreement with previous research, we find that the most energetic shock waves are emitted by highly spherical collapses, reaching up to about 90% of the initial bubble energy. The bubbles here are found to emit a single shock front at anisotropies up to $\zeta \approx 10^{-3}$ (equivalent to $\gamma \approx 14$), which is also the approximate limit for the appearance of a microjet piercing the bubble in our setup [30].

In the last stages of the collapse, the pressure in the liquid near the bubble wall increases to values so high that it deflects light, producing the shaded ring around the bubble in Fig. 4(a) (frames 2–4). This pressure has previously been predicted to reach thousands of bars [14,35] and experimentally detected using Mach-Zehnder interferometry [41] or elevated ambient pressures [42]. However, it is interesting that our setup is able to visualize it using simple shadowgraphy at atmospheric pressure.

This is due to the bubble's high initial sphericity allowing it to reach very small radii upon its exceptionally spherical collapse.

The incompressible model for the pressure distribution around the bubble, developed by Rayleigh a century ago, is given as follows [35]:

$$\frac{p}{p_0} = 1 + \frac{R}{3r}\left(\frac{R_0^3}{R^3} - 4\right) - \frac{R^4}{3r^4}\left(\frac{R_0^3}{R^3} - 1\right) \tag{3}$$

where r is the radial distance from the bubble center. Considering the lower bound for the compression ratio of the bubble in Fig. 4(a) ($R_0/R_{\text{min}} > 40$), we expect the maximum peak pressure to be on the order of GPa in the incompressible framework. The pressure buildup is visible in the hydrophone signal in Fig. 4(b) as a relatively slow rise preceding the peak pressure of the shock. We may compute the pressure evolution in time from Eq. (3) at the radial distance where the hydrophone is located ($r = 44.5$ mm), assuming the time evolution of the bubble radius to follow the analytical approximation $R(t) \approx R_0(1 - t^2)^{2/5}$ [43] (where t is the time normalized to collapse time T_c), down to $R_{\text{min}} \approx 100$ μm. The computed pressures from Eq. (3) can be roughly compared with the hydrophone signal if the delay in the far field caused by the finite sound speed is accounted for. Furthermore, the shock pressure peak is assumed to represent a time approximately 100 ns preceding the final collapse instant, for the shock wave is expected to propagate the first $\sim$300 μm with supersonic speeds [37]. The average shock speed during the exposure of the first frame after the collapse is estimated approximately as 3000 ms^{-1} from Fig. 4(a) and therefore the shock wave is indeed estimated to reach the hydrophone $\Delta t \approx 102$ ns earlier than the pressure buildup, of which the information is assumed to propagate at the sound speed. As can be seen in Fig. 4(b), the computed (dashed line) and measured (solid line) pressure evolutions almost up to the signal peak are surprisingly similar. The good agreement is remarkable considering our unconventional pressure calibration. The model is not able to reproduce the shock wave because it is incompressible (dotted line), and when the bubble reaches a radius of $R = 100$ μm, the predicted pressure at the hydrophone location is $p - p_0 = 3.8$ MPa, which is close to the measured peak pressure very likely by coincidence. The pressure rise, in addition to the tensile part of the shock wave tail, is the clearest difference between the measured waveform from a spherical collapse and that of the bubble generation (Fig. 2).

B. Nonspherical collapse: Bubbles near a free surface

The dynamics of bubbles near free surfaces has been extensively studied in the past experimentally, theoretically, and numerically [28,44–50], yet no study to date has focused specifically on their shock wave emission. The advantage of studying bubbles near a free surface is the contact avoidance between the bubble and the surface, allowing thus free collapse and rebound dynamics, as the bubble migration and the microjet are directed away from the surface (contrary to a rigid surface). While bubbles near a free surface form microjets that have characteristics similar to bubbles deformed by a rigid surface [30], their shapes at the final collapse stages have significant differences, which may give us some further insight into the distinct shock wave emission mechanisms. In particular, for $\gamma = 1-3$, the microjet formed during the collapse is broad and impacts the opposite bubble wall on a ring rather than a single point, some examples being illustrated in Fig. 5. At lower values of γ, the microjet becomes narrow and the spike formed on the free surface increases in height. The shapes in Fig. 5 were obtained numerically using potential flow theory (boundary integral method [30,46,48,51,52]) and have previously been validated by their good agreement with experiments [30].

We now present observations of shock waves from bubbles collapsing near a free surface at different levels of ζ. Nonspherically collapsing bubbles that produce microjets generate multiple shock waves, which are clearly observed on the shadowgraph images at $\zeta > 10^{-3}$. However, they only become clearly distinct events on the hydrophone signal beyond $\zeta \sim 8 \times 10^{-3}$ ($\gamma \sim 5$).

Figure 6 shows selected shadowgraph images and the corresponding hydrophone pressures for a bubble collapsing at $\zeta = 3.8 \times 10^{-3}$. The first sign of asymmetry in the bubble collapse, together

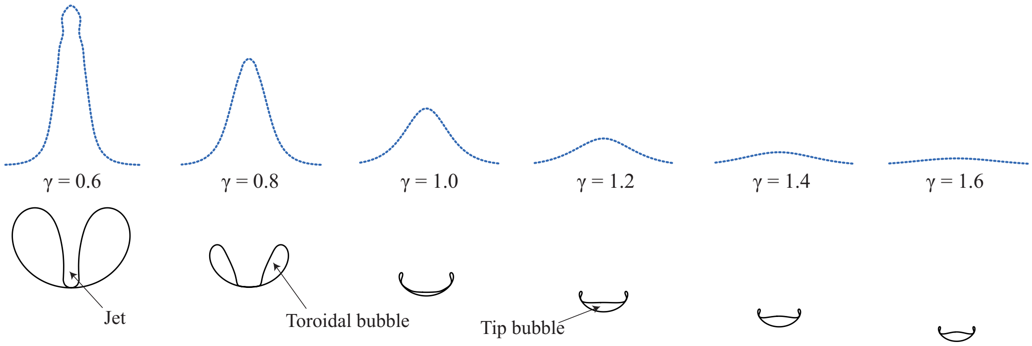

FIG. 5. Illustration of the bubble shapes at jet impact for different standoff distances γ from the free surface. The corresponding values for ζ from left to right are $\zeta = 0.54$, 0.30, 0.20, 0.14, 0.10, and 0.076. The shapes of the free surface are shown as a dotted line. The shapes have been obtained numerically using potential flow theory.

with the bubble's displacement, is the shaded region appearing near the upper bubble wall where the downward microjet is forming [starting from frame 2 in Fig. 6(a)]. It is similar to the gradual pressure buildup observed for the spherical collapse in Fig. 4(a), but not spherically symmetric. It is also in agreement with reported numerical simulations of jetting bubbles, finding higher pressures at the root of the jet relative to the rest of the pressure field [27–29,53]. The shaded region eventually surrounds most of the bubble in frame 5 and two clear shock fronts are visible in frame 6 following the collapse. We observe luminescence at the tip of the bubble in frame 5, which also appears to be the center of the most pronounced shock wave visible in the subsequent images. Although it is much weaker compared to the light emitted in the spherical case, the observed flash suggests a high gas compression between the jet and the opposite bubble wall. Interestingly, the first shock front in Fig. 6(a) is produced on the side of the bubble where the initial pressure rise in the liquid occurred. The hydrophone is unable to distinguish the first shock wave from the rest due to its location and temporal resolution, but it records the gradual pressure rise occurring on the sides of the bubble preceding the main shock wave [Fig. 6(b)].

Figures 7(a)–7(h) show images and the corresponding measured shock pressures for more deformed bubbles, collapsing at different distances from the free surface at $\zeta = 2.9 \times 10^{-2}$,

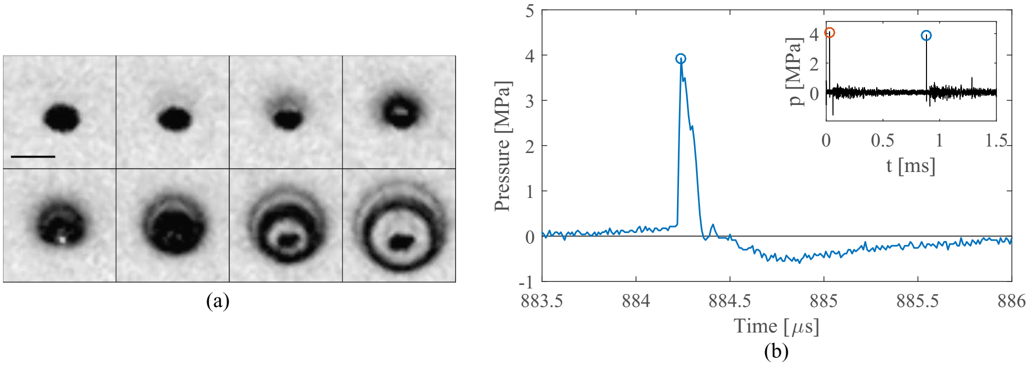

FIG. 6. Cavity of $R_0 = 4.1$ mm at $\zeta = 3.8 \times 10^{-3}$ ($\gamma = 7.2$). (a) High-speed shadowgraph visualization. The interframe time is 100 ns and the black bar shows the 1-mm scale. (See [39] for the corresponding movie.) (b) Pressure recorded by the hydrophone. The inset shows the whole bubble oscillation, where the orange and blue circles refer to generation and collapse shock wave peak pressures, respectively.

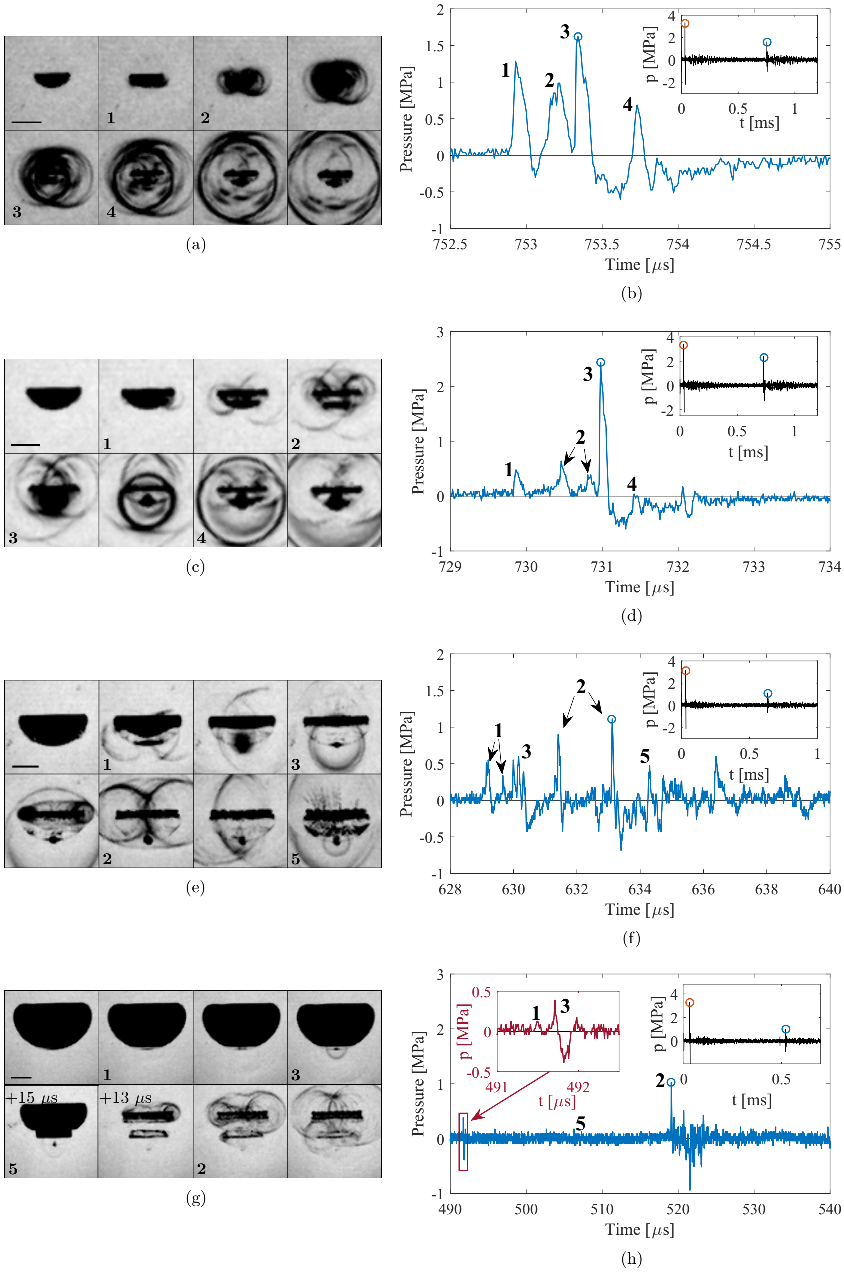

FIG. 7. Selected images (left) and hydrophone signal (right) for cavities of (a) and (b) $R_0 = 3.6$ mm at $\zeta = 2.9 \times 10^{-2}$ ($\gamma = 2.6$), (c) and (d) $R_0 = 3.6$ mm at 4.6×10^{-2} ($\gamma = 2.1$), (e) and (f) $R_0 = 3.2$ mm at $\zeta = 0.19$ ($\gamma = 1$), and (g) and (h) $R_0 = 3.0$ mm at $\zeta = 0.33$ ($\gamma = 0.77$) for an interframe time of (a) 200 ns, (c) 300 ns, (e) 600 ns, and (g) 400 ns unless otherwise indicated. The shock waves are denoted by 1, jet impact; 2, torus collapse; 3. tip bubble collapse; 4, second torus collapse; and 5, second tip bubble collapse shock waves. The black bars show the 1-mm scale. The insets show the whole bubble oscillation, where the orange and blue circles refer to generation and collapse shock wave peak pressures, respectively. (See [39] for the corresponding movies. For the bubble at $\zeta = 0.33$, the movie combines films made of two separate bubbles due to the long duration of the events and the limited number of frames captured by the camera. The events are highly repetitive.)

4.6×10^{-2}, 0.19, and 0.33. The recorded peak pressures are significantly lower compared to the more spherical cases and many distinct shock wave events are observed. The first pressure peak in all cases corresponds to the water hammer induced by the jet impact. Such a shock has been observed in the past for nonspherically collapsing bubbles both experimentally [19,23,24] and numerically [26,28]. It produces a toruslike shock wave due its contact on the opposite bubble wall not being a single point but a circular line (see Fig. 5), clearly visible on the images as two shock source points on the sides of the bubble. If the jet is broad enough, the hydrophone may detect two individual pressure peaks, such as in Fig. 7(f), owing to such toruslike shock having two fronts on the hydrophone axis that reach the sensor. Subsequently, the jet separates a part of the vapor at the tip from the rest of the bubble, with this separation being particularly clear in Figs. 7(c) and 7(e) as a horizontal line that cuts the bubble and implies that the vapor in that zone has disappeared. It is difficult to tell with certainty that the first shock wave results from a jet impact in Fig. 7(a) due to the short time intervals between the distinct events. However, observing several bubbles between $\zeta = 2.9 \times 10^{-2}$ and 4.6×10^{-2} (of which the results are summarized later in Sec. III C), a systematic variation of the shock timings and strengths with ζ was noted. The identification of each peak in Fig. 7(b) was therefore done accordingly. The peak pressure associated with the jet impact decreases with an increasing ζ and is barely detected at $\zeta = 0.33$. At $\zeta = 2.9 \times 10^{-2}$ and 4.6×10^{-2} [Figs. 7(a)–7(d)], the jet impact is followed by the collapse of the toroidal bubble. The associated shocks are toruslike and meet in the jet axis in the middle of the bubble, which is known to sometimes produce a counterjet, a vertical columnlike cluster of microcavities [23,30]. The torus collapse shock may also yield two individual peaks in the pressure signal, such as in Figs. 7(d) and 7(f). The peak pressure of the torus collapse shock first decreases with increasing ζ [Figs. 7(b) and 7(d)] and then increases again slightly [Figs. 7(f) and 7(h)]. The next pressure peak in Figs. 7(b) and 7(d) corresponds to the tip bubble collapse. It appears to be the dominant shock in the collapse scenario at these ζ. The tip bubble collapse shock triggers a second collapse of the rebounding toroidal bubble, which emits a further shock wave manifested as the fourth pressure peak in the signal. The second torus collapse pressure peak is considerable at $\zeta = 2.9 \times 10^{-2}$ but barely detected by the hydrophone at $\zeta = 4.6 \times 10^{-2}$. As can be seen in Figs. 7(e) and 7(g), at a higher ζ the tip bubble collapse and the torus collapse change order. In Fig. 7(g) the tip bubble is very small and its collapse follows the jet impact so closely that it is difficult to distinguish the shocks they emit. At $\zeta = 0.19$ it is the torus collapse that triggers a second collapse of the tip bubble, while at $\zeta = 0.33$ the tip bubble is able to collapse naturally a second time long before the torus collapse. In Fig. 7(g) the compression of the toroidal bubble is highly nonuniform, yielding multiple peaks that generate a noisy hydrophone signal [Fig. 7(h)].

The shock wave strengths are also visible as the darkness levels of the corresponding image pixels owing to their ability to deflect light, which can be seen, for example, in Fig. 7(c) where the tip bubble shock wave is clearly the most pronounced of all the events. The time intervals between each event substantially increase with ζ. When the bubble collapses very close to the free surface, the hydrophone also detects the reflected rarefaction waves following closely the original shocks and contributing to the noise in the signal of Fig. 7(h). These waves are visible in all movies of Fig. 7 and, due to their negative pressure resulting from the reflection at the free surface, they generate secondary cavitation in the bubble's neighborhood, as shown in Fig. 8. The secondary cavities are visible as clusters of microbubbles most prominently in the path of the focused laser, where the liquid is preheated and thereby the nucleation of cavities is facilitated, and between the bubble and the free surface [Fig. 8(b)]. Interestingly, some of these clusters, arranged in streamers towards the central axis of the toroidal bubble, delineate the flow induced by the formation of the microjet. The vertical column of microbubbles between the toroidal bubble and the free surface in Fig. 8(b) appears to result from the confluence of the rarefaction waves that are the reflections of the shocks initially emitted by the torus collapse. For the same bubble, secondary cavitation resulting from the shock emitted at the first tip bubble collapse is also observed below the bubble, right after the jet impact, as can be seen in Fig. 8(a). Here the negative pressure results from the reflection at the bubble interface, and the rarefaction wave follows closely the original shock wave, which explains the significant tensile tail of the tip bubble collapse peak captured by the hydrophone in Fig. 7(h).

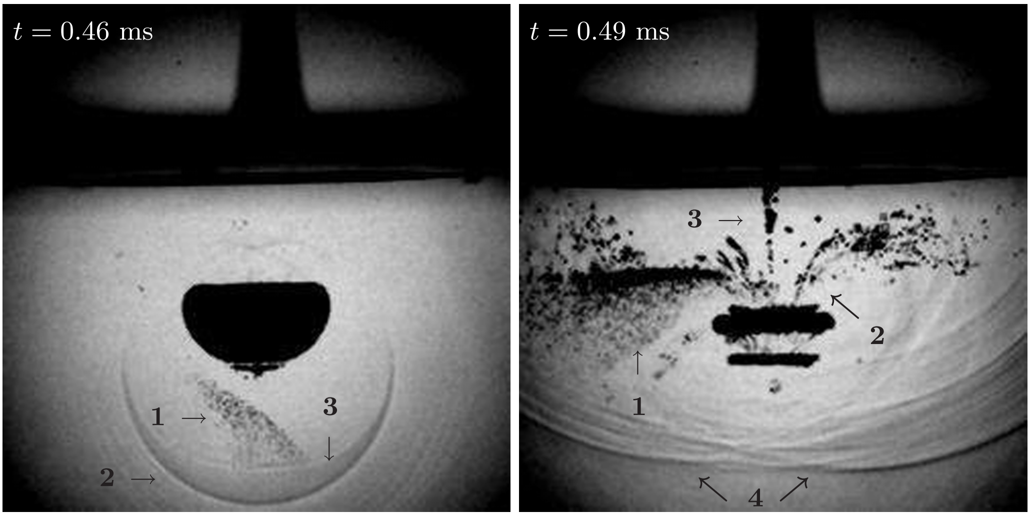

(a) (b)

FIG. 8. Visualization of secondary cavitation resulting from the passage of rarefaction waves for the same bubble as in Fig. 7(g) at two different instants: (a) secondary cavitation (1) below the bubble, generated by the tip bubble collapse shock wave, (2) turned into a rarefaction wave, and (3) after reflecting at the bubble's interface and (b) secondary cavitation visible (1) in the preheated cone-shaped zone in the laser path, (2) as streamers along the microjet flow and (3) as a vertical column, and (4) generated by the rarefaction waves caused by the reflection of torus collapse shock waves at the free surface. (See [39] for the corresponding movie.)

C. Energy distribution and event timings

The observations of the distinct shock wave events and their corresponding pressures show important variations with different bubble asymmetries. The energy of the observed shock waves can be estimated from the hydrophone pressure signal via Eq. (2), where the integration range is selected by identifying the pressures associated with each individual event from the high-speed visualizations. It should be noted that this method assumes spherically symmetric propagation of the shock wave. Some shocks, especially the jet impact shock, might have some directionality, biasing their energy measurement. Indeed, it has been shown numerically that jet impact-induced shocks are dependent on the orientation with respect to the jet close to the bubble [20,26]. However, the symmetric shock shadings seen in the high-speed visualizations far from the bubble center (not shown in figures) suggest that this directionality must be subdominant. The shock pressure dependence on orientation likely reduces as the wave propagates and decreases in amplitude. We nonetheless caution that directionality is a potential source of systematic error, which might be reduced in future experiments by using multiple hydrophones in different directions.

The fraction of the bubble's initial energy E_0 distributed to the distinct shock waves for bubbles collapsing near a free surface is shown in Fig. 9 as a function of the anisotropy parameter ζ (and the equivalent γ). We only measured bubbles up to $\zeta \sim 0.3$ ($\gamma \sim 0.8$), beyond which the free surface resulted in severe perturbations in the hydrophone signal due to the reflected rarefaction waves. The driving pressure was kept at $\Delta p > 75$ kPa in order to avoid simultaneous deformations by the free surface and gravity, which could lead to more complex shapes at the bubble collapse (e.g., bubble splitting or annular jets [54]). The energy of each of the three main shock waves, i.e., jet impact, tip bubble collapse, and torus collapse, vary as functions of ζ. Interestingly, each of them dominates a certain range of ζ, as can be seen in Fig. 9. For bubbles that produce jets, the jet impact shock appears to dominate up to $\zeta \sim 2 \times 10^{-2}$. The tip bubble shock wave has a clear domination in the range $2 \times 10^{-2} < \zeta < 0.15$. Beyond $\zeta \sim 0.15$, the torus collapse shock wave is the most

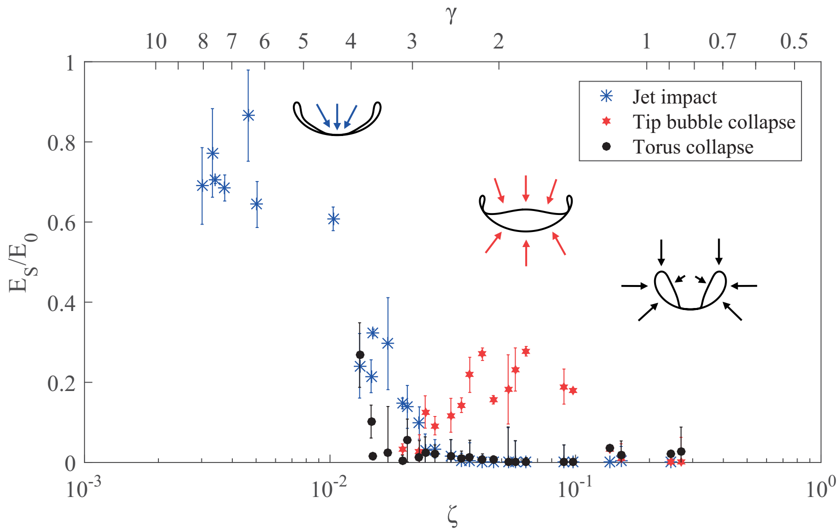

FIG. 9. Normalized shock wave energy for each shock emission mechanism from bubbles deformed by a near free surface, as a function of ζ (and corresponding γ, top axis). Numerically calculated bubble shapes at jet impact are shown for $\zeta = 10^{-2}$, 6×10^{-2}, and 0.3.

energetic, yet weak in relative terms with less than 10% of the initial bubble energy. The torus collapse energy is particularly low in the range $2 \times 10^{-2} < \zeta < 0.1$, coinciding with the domination of the tip bubble. The second torus collapse and the second tip bubble collapse emit shock waves with a negligible energy compared to the others, which is why they have been excluded from the figures.

The domination of the tip bubble in the range $2 \times 10^{-2} < \zeta < 0.15$ is explained through its large volume relative to the rest of the bubble at the moment of the jet impact, its spherical topology that allows an effective gas compression during its collapse, and/or the further compression provided by the pushing jet. The large volume of the tip bubble and the small volume of the torus in this range result from the characteristic shape the jet assumes for bubbles collapsing near a free surface (see Fig. 5). Beyond $\zeta \sim 0.1$ however, the torus becomes relatively larger again at the moment of jet impact, as the bubble shape at $\zeta = 0.3$ in Fig. 9 suggests, and the torus is able to compress the gases it contains more effectively. This explains the slight rise of the torus collapse shock energy for $\zeta > 0.1$.

When the energies of the different collapse shock waves are summed, an overall decrease of the total shock energy is observed, as can be seen in Fig. 10. Here data for lower ζ have been added, including energies from pressure measurements for which it was not possible to distinguish the different shock wave events. Interestingly, the total shock energy varies as a function of ζ independently of the bubble maximum radius and driving pressure within the ranges covered here ($R_0 = 1{-}4$ mm and $\Delta p = 0.75{-}1$ bar). A major part of the collapse shock energy decrease occurs within the range $10^{-3} < \zeta < 2 \times 10^{-2}$, where the jet impact hammer shock is expected to dominate. As the bubble deforms, the liquid inflow towards the bubble center becomes anisotropic and as a result, the level of compression of the bubble's enclosed gases reduces yielding weaker shock wave emission. As less energy is radiated away by the shock waves for increasing ζ, more energy is distributed to the motion of the liquid forming the microjet and to the rebound bubble, both of which are observed to grow with ζ.

The timing of the distinct events in the shock wave scenario also appears to vary with the level of deformation of the bubble. Figure 11 displays the time difference ΔT between the jet impact, which generally emits the first shock wave, and the other observed events, normalized to the bubble

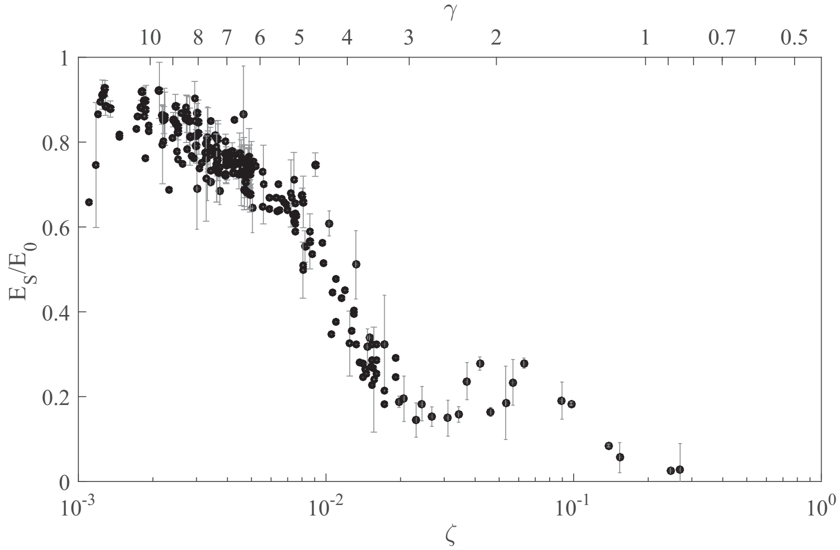

FIG. 10. Normalized total collapse shock wave energy E_S/E_0 for bubbles deformed by a near free surface, as a function of ζ (and γ, top axis).

collapse time T_c. The experiments are displayed together with our previously established model estimating the normalized time between the jet impact and torus collapse $\Delta T/T_c = 0.15\zeta^{5/3}$ [30]. Only data for $\zeta > 10^{-2}$ are displayed as the temporal resolution of our apparatus is not sufficient for identifying the exact shock timings of more spherical bubbles. The jet impact occurs within the last 1% of the bubble's collapse time up to $\zeta \approx 0.2$, followed very closely by the other events. The torus collapse precedes the tip bubble collapse up to $\zeta \approx 0.14$, beyond which they change order.

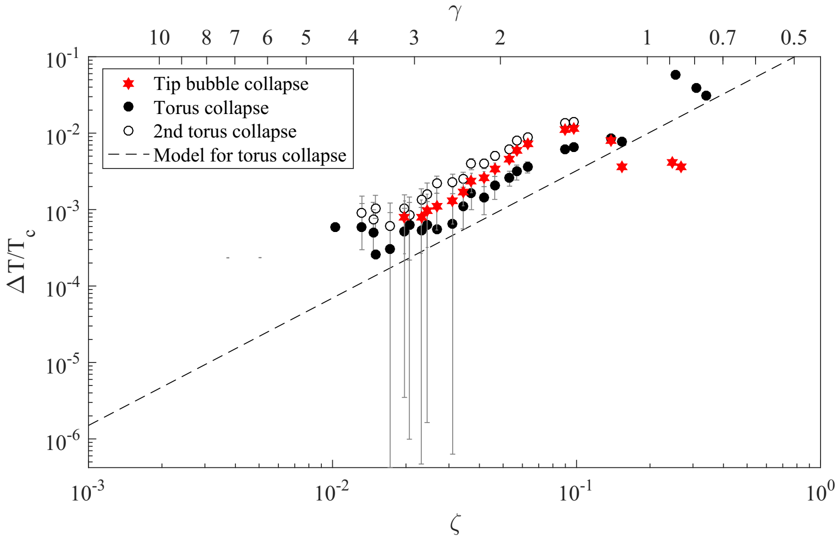

FIG. 11. Time differences between the jet impact and the tip bubble collapse, torus collapse, and second torus collapse as a function of ζ (and γ, top axis), normalized with bubble collapse time T_c. The time between jet impact and torus collapse is modeled as $\Delta T/T_c = 0.15\zeta^{5/3}$ [30].

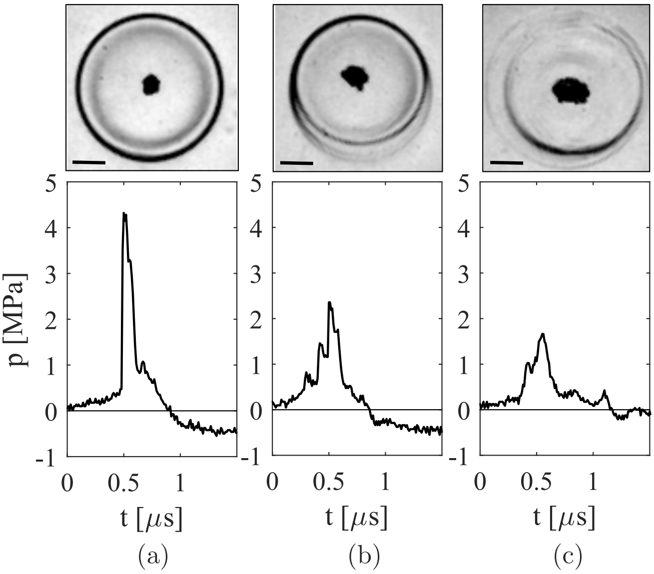

FIG. 12. Examples of hydrophone pressure signals of shock waves measured at the collapse of bubbles deformed by gravity at (a) $\zeta < 10^{-3}$, (b) $\zeta = 3.8 \times 10^{-3}$, and (c) $\zeta = 10^{-2}$. The corresponding shadowgraph images with an exposure of 50 ns are shown on top. The black bars show the 1-mm scale.

The second torus collapse occurs right after the tip bubble collapse up to this limit, as the rebounding torus compresses under the effect of the shock wave produced by the latter, which is seen as an almost constant time difference between the two events in Fig. 11. The normalized timings of each shock wave are independent of the maximum bubble radii and driving pressures covered here.

IV. MODELS FOR SHOCK ENERGY AND PRESSURE

We now investigate shock waves from nonspherically collapsing bubbles at a more general level with the aim of developing a semiempirical model to predict their strengths. For this purpose, we look at shock waves from bubbles deformed by different sources, in particular by the gravity-induced uniform pressure gradient. Examples of measured shock waves from bubbles deformed by gravity are shown in Fig. 12. A spherical collapse [Fig. 12(a)] produces a single shock, as observed previously in Sec. III A. Nonspherical collapses [Figs. 12(b) and 12(c)] generate multiple shocks and the associated peak pressures clearly decrease with increasing bubble deformation, similarly to bubbles deformed by a free surface. However, the characteristic shape of bubbles collapsing in uniform pressure gradients is such that the radii of curvature of the jet tip and the opposite bubble wall at their impact are very similar for a wide range of ζ according to potential flow theory [30], as illustrated in Fig. 13 for $\zeta = 10^{-2}$. As a consequence, the volumes of the tip bubble and the toroidal bubble remain relatively small and the associated shocks are barely distinguishable. We therefore analyze the collapse shock as one event, expected to be dominated by the jet impact (as suggested by Fig. 9 for bubbles near a free surface at $\zeta < 10^{-2}$), without resolving its substructure in the following analyses.

We first consider the variation of the peak pressures $p_{\max}$ measured by the hydrophone as a function of ζ. Figure 14 shows this function for bubbles deformed by the gravity-induced pressure gradient (varied parameters $R_0 = 1.5-10$ mm, $\Delta p = 6-98$ kPa, at normal gravity). Clearly, the relation between $p_{\max}$ and ζ depends on Δp. We can build a model for the relationship between $p_{\max}$, Δp, and ζ, based on the simplistic assumptions of scale-free microjets and shocks resulting

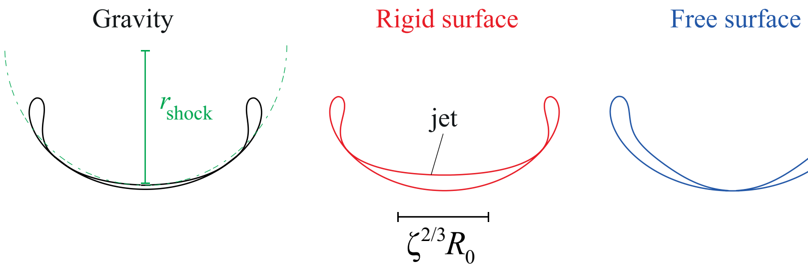

FIG. 13. Bubble shapes at jet impact for bubbles deformed by a uniform pressure gradient, a near rigid surface, and a near free surface, predicted by potential flow theory [30] for $\zeta = 10^{-2}$. Here $\boldsymbol{\zeta}$ is directed downward.

from a water hammer pressure caused by the jet impact [10,26]:

$$p_h = \tfrac{1}{2}\rho c U_{\rm jet} = 0.45(\rho c^2 \Delta p)^{1/2}\zeta^{-1}, \tag{4}$$

where $U_{\rm jet}$ is the microjet speed at its impact on the opposite bubble wall. The scaling model for the microjet speed $U_{\rm jet} = 0.9(\Delta p/\rho)^{1/2}\zeta^{-1}$ has previously been established by combining numerical simulations and analytical arguments with experimental observations and is a valid approximation for jets driven by gravity and near surfaces at $\zeta < 0.1$ [30]. We can therefore expect also the resulting hammer pressures to be similar for these different sources of bubble deformation and to decrease with ζ for a given Δp (with constant ρ and c). The scaling factor in Eq. (4) could be different if the jet impact is not the dominant shock mechanism, but this is irrelevant in the following derivation because of the free parameter α discussed hereafter.

The equivalent observational proxy for p_h is expressed as

$$p_h = p_{\rm max}\left(\frac{d}{r_{\rm shock}}\right)^{\beta} = \alpha p_{\rm max}\left(\frac{d}{R_0}\right)^{\beta}\zeta^{-2\beta/3}, \tag{5}$$

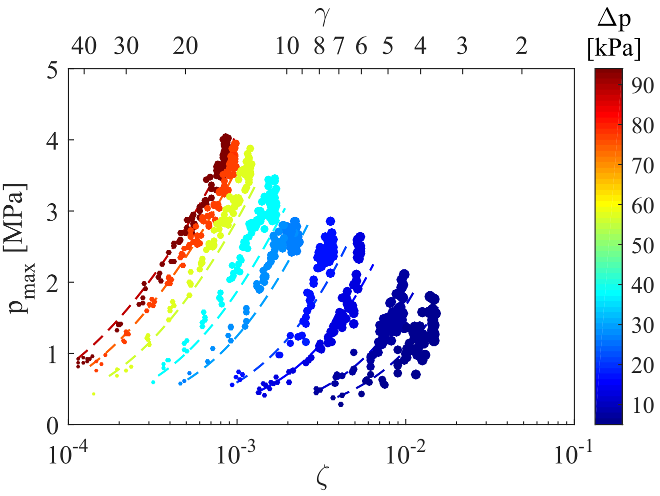

FIG. 14. Measured shock peak pressures as a function of ζ (and γ, top axis) for bubbles deformed by gravity. The dashed lines represent the model in Eq. (6). The colors indicate different driving pressures Δp. The symbol sizes portray the different maximum bubble radii.

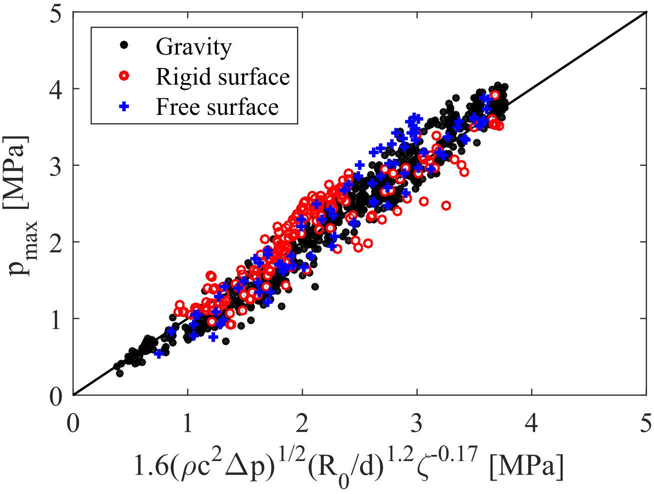

FIG. 15. Measured shock wave peak pressures as a function of the model given in Eq. (6) for bubbles deformed by gravity, a rigid surface, and a free surface.

where $p_{\max}$ is the peak pressure measured by the hydrophone, d is the distance between the bubble center and the hydrophone sensor, r_{shock} is the shock emitting radius, assumed to scale as the radius of the jet tip (see schematic in Fig. 13) and thereby as the bubble's characteristic length at jet impact $s \propto \zeta^{2/3}R_0$ as predicted by potential flow theory for $\zeta \ll 1$ [30], and α and β are free parameters. Here α represents the unknown scaling of $r_{\text{shock}} \propto \zeta^{2/3}R_0$. In addition, β would equal 1 for negligible shock dissipation and spreading of the shock width, yet in reality nonlinearities are present and result in a higher exponent, typically about 2 in the near field and ~1.1 in the far field of the emission center [1,37,55,56]. Equating Eqs. (4) and (5) gives

$$p_{\max} = \frac{0.45}{\alpha}(\rho c^2 \Delta p)^{1/2}\left(\frac{R_0}{d}\right)^{\beta}\zeta^{2\beta/3-1}. \tag{6}$$

We fit α and β simultaneously to a sample of 931 bubbles deformed by gravity to minimize the χ^2 deviation between the left- and right-hand sides of Eq. (6) [57]. The resulting fitted parameters are $\alpha = 0.277 \pm 0.006$ and $\beta = 1.249 \pm 0.003$ and the corresponding determination coefficient is $R^2 = 0.93$. As expected, β lies between 1 and 2. In the case of bubbles deformed by gravity, there is a unique relation between R_0, Δp, and ζ as shown by Eq. (1). Substituting R_0 from this relation into Eq. (6) makes $p_{\max}$ a function of only Δp and ζ. These relations are plotted as dashed lines in Fig. 14 and show excellent agreement with the measurements.

The lines in Fig. 14 can be collapsed to a single relationship by plotting the measured peak pressures $p_{\max}$ directly against the model in Eq. (6), which is shown in Fig. 15. We now also apply this simple model to predict the shock pressures of nonspherical bubbles with different sources of deformation (free and rigid surfaces), where the unique relationship between R_0, Δp, and ζ no longer holds because of the additional dependence on the distance h to the surface, as shown by Eq. (1). These data also coincide with the model, as can be seen in Fig. 15, confirming that the hammer pressure model can be used to estimate shock pressures produced by a nonspherical bubble collapse. The pressures p_h at the source, estimated using Eqs. (4) and (5), range from 100 MPa to 10 GPa at $\zeta > 10^{-3}$.

Figure 16 displays the normalized collapse shock wave energy for bubbles deformed by gravity, a nearby rigid surface, and a free surface as a function of ζ. All the measured shock energies generally decrease with increasing ζ independently of R_0 and Δp. For gravity-deformed bubbles, most of the decrease happens in the range $10^{-3} < \zeta < 10^{-2}$, reaching values down to about 10% of initial

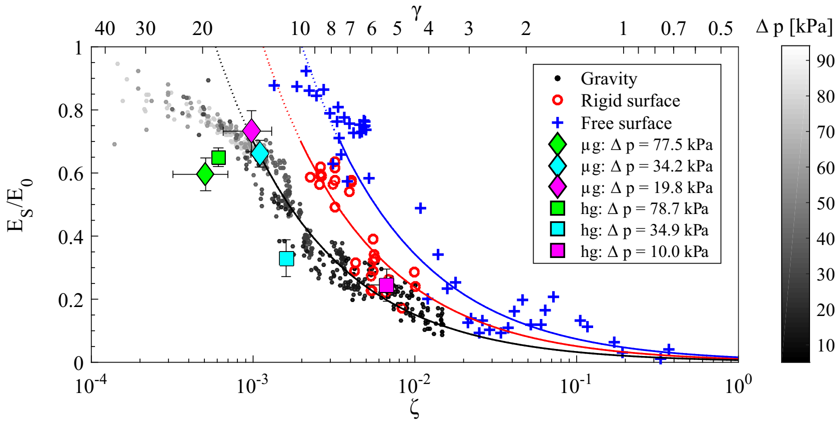

FIG. 16. Normalized total collapse shock wave energy for bubbles deformed by gravity, a near rigid surface, and a near free surface as a function of ζ (and γ, top axis). Averaged shock energies measured in microgravity (μg) ($0 \pm 0.02g$) and hypergravity (hg) ($1.66g \pm 0.093g$) at three different Δp are also displayed. The grayscale indicates different driving pressures Δp for bubbles deformed by gravity. The models in solid lines show the fits $0.0073\zeta^{-2/3}$, $0.011\zeta^{-2/3}$, and $0.016\zeta^{-2/3}$ for bubbles deformed by gravity, a rigid surface, and a free surface, respectively. The mean error of E_S/E_0 is 0.04.

bubble energy E_0 at $\zeta \sim 10^{-2}$. These values differ significantly from bubbles deformed by a rigid and a free surface that respectively have shock energies as high as 30% and 40% of the initial bubble energy E_0 at $\zeta \sim 10^{-2}$ ($\gamma \sim 4.4$). Shocks from bubbles deformed by a near rigid and a free surface experience a decrease in energy with ζ that is similar to the gravity-deformed cases, but which occurs at a higher ζ.

It should be noted that the expression of ζ for gravity-induced bubble deformations [Eq. (1)] includes Δp, making Δp correlate with ζ in our data obtained on ground (see the grayscale in Fig. 16). However, the data in microgravity ($0 \pm 0.02\,g$), which were obtained aboard European Space Agency parabolic flights, confirm that the bubble deformation is the main cause of the observed shock energy variations, rather than Δp. For example, bubbles collapsing at $\Delta p \approx 20$ kPa in our experiment on ground emit low-energy shocks ($E_S/E_0 < 30\%$), yet in microgravity at the same driving pressure $E_S/E_0 > 75\%$ [58]. Some data for bubbles collapsing at higher gravity levels ($1.66g \pm 0.093g$) are also displayed in Fig. 16, showing reasonable agreement with the general shock energy trend with ζ.

Since the measured peak pressures for deformed bubbles are well approximated with the hammer pressure model, we aim at estimating their shock energies using the same approach. We recall that the shock energy $E_S = (4\pi d^2 \rho^{-1} c^{-1}) \int p^2 dt$ from Ref. [18], as for Eq. (2). If the pressure profile in time is represented with a hammer pressure p_h being applied for a time $\Delta t = \Delta d c^{-1}$, where Δd denotes the thickness of the shock, the energy reads $E_S = (4\pi d^2 \rho^{-1} c^{-1}) p_h^2 \Delta t$. The shock wave energy is therefore alternatively expressed as

$$E_S = \frac{\Delta V p_h^2}{\rho c^2}, \tag{7}$$

where $\Delta V = 4\pi d^2 \Delta d$ is the volume of the compressed liquid. As mentioned before, the characteristic length of the bubble at the jet impact scales as $s/R_0 \propto \zeta^{2/3}$. As the surface area of contact of the jet onto the opposite bubble wall is two dimensional and the compressed liquid volume is assumed to be proportional to that area, we have $\Delta V/R_0^3 \propto s^2/R_0^2 \propto \zeta^{4/3}$. With this model plugged into Eq. (7) and p_h substituted for Eq. (4), we obtain

$$\frac{E_S}{E_0} \propto \frac{\Delta V}{R_0^3 \zeta^2} \propto \zeta^{-2/3}. \tag{8}$$

The missing scaling factor for Eq. (8) comes from the unknown size of the compressed liquid region. An analytical evaluation of this unknown is difficult and would have to account for the nonuniform liquid compression by the curved jet tip. The scaling factor is expected to vary for the distinct sources of deformations, since the jet shapes are different for each case and leave gas or vapor pockets of dissimilar sizes between the jet and the opposite bubble wall, as illustrated in Fig. 13 for $\zeta = 10^{-2}$. These vapor pockets are rather large for bubbles collapsing near a rigid or a free surface, while gravity-induced jets hit the opposite bubble wall in a highly uniform way, thereby resulting in the smallest scaling factor. When minimizing the χ^2 deviation between the measurements E_S/E_0 for bubbles deformed by gravity at $\zeta > 10^{-3}$ and a model in the form $f = a\zeta^b$ with free parameters a and b, we find $a = 0.0078$ and $b = -0.66$. When imposing $b = -2/3$ to conform with Eq. (8), the best fit for a is 0.0073. The corresponding fitted scaling factors for the rigid and free surfaces are $a = 0.011$ and 0.016, respectively. Equation (8) with these fitted scaling factors is plotted as solid lines for bubbles deformed by gravity, a free surface, and a rigid surface in Fig. 16 and agrees reasonably well with the experimental data.

V. DISCUSSION

There are several limitations in the presented shock models worth addressing. The microjet is expected to reach the speed of sound for a bubble collapsing at $\zeta \lesssim 0.9(\Delta p/\rho)^{1/2}c^{-1}$ ($\zeta \lesssim 0.006$ at $\Delta p = 98$ kPa), below which the model in Eq. (4) may no longer be able to estimate the jet hammer pressures. Furthermore, our model neglects the gas inside the bubble. Compressed and heated gases within highly spherically collapsing bubbles can potentially slow down and destroy the jet and/or delay or prevent its formation. These effects naturally decrease with increasing ζ, since at higher ζ the jet forms earlier in the bubble evolution, when the gases are less compressed. We estimate the bubble gas to seriously hamper the jet for $\zeta < 10^{-3}$, where no observable jets are formed in the bubble rebound in our current setup [30]. This is the likely explanation for the sudden curvature change in the shock energy trend for bubbles deformed by gravity at $\zeta \sim 10^{-3}$, as can be seen in Fig. 16. Below this approximate threshold (at which $p_h \sim 7$ GPa for bubbles collapsing here at atmospheric pressure), the shock pressures predicted by the model are overestimated. This threshold value is consistent with previous findings for a spherical collapse at atmospheric pressure, both in our setup (Sec. III A) and in the literature [1,2,59].

The shock energies of bubbles collapsing near a rigid surface show important differences when compared with the measurements performed by Vogel and Lauterborn [18]. Although they observed, similarly to us with bubbles near a free surface, a clear minimum in shock energies at $\gamma = 1$, they also measured shocks beyond $\gamma \sim 3$ to have the same energies as those emitted in a spherical collapse, while at $\gamma = 3$ we measure barely 20% of a typical shock energy from a spherical collapse. This suggests that the experimental conditions play an important role in the collapse shock wave characteristics, including the initial bubble sphericity, which highly differs for parabolic mirror- and lens-based laser focusing methods. Indeed, in Vogel and Lauterborn's study the standoff was varied only up to $\gamma \sim 3$, beyond which a spherical collapse was assumed, while we still find important shock energy variations between $\gamma \sim 5$ and 10.

VI. CONCLUSION

We have presented detailed observations of shock wave emissions from the collapse of bubbles with various levels of deformation, quantified by the anisotropy parameter ζ, using simultaneous time-resolved shadowgraphy and needle hydrophone pressure measurements. A gradual pressure rise in the liquid near the bubble wall was observed in the last collapse stage of nearly spherically collapsing bubbles, in agreement with the century-old predictions of Lord Rayleigh. Nonspherical bubble collapses produced multiple shock waves associated with different processes such as the jet impact and the individual collapses of the various separated parts of the bubble. When quantifying these distinct shocks for bubbles collapsing near a free surface, the jet impact shock was found to dominate up to $\zeta \sim 2 \times 10^{-2}$, the bubble tip collapse in the range $2 \times 10^{-2} < \zeta < 0.15$, and the torus collapse at $\zeta > 0.15$. The timings of the individual events, normalized with the bubble collapse time, were also found to vary with ζ.

Models predicting the shock peak pressure and energy were proposed based on the assumption that the shock wave is generated by a jet impact hammer pressure. The pressure model showed excellent agreement with the observed data in the range $10^{-3} < \zeta < 10^{-2}$ for all three sources of bubble deformation used here (gravity, rigid surface, and free surface) and the energy model captured the approximative trend of the measured energies. The total collapse shock wave energy, normalized to the total bubble energy, generally decreased with increasing ζ. However, we found differences between the shock energies from bubbles deformed by different sources, which likely result from the small variations in the jet shapes at their impact onto the opposite bubble wall. Interestingly, these differences do not seem to affect the shock peak pressures, which could be due to the jet speed at the moment of impact (which the hammer pressure is proportional to) being nearly identical for the three sources of bubble deformation at this range of ζ.

ACKNOWLEDGMENTS

We acknowledge the support of the Swiss National Science Foundation (Grant No. 200020-144137), the University of Western Australia Research Collaboration Award obtained by D.O. and M.F., the European Space Agency for the 60th and 62nd parabolic flight campaigns, and Professor Ullrich for the first Swiss parabolic flight.

---

[1] R. Pecha and B. Gompf, Microimplosions: Cavitation Collapse and Shock Wave Emission on a Nanosecond Time Scale, Phys. Rev. Lett. **84**, 1328 (2000).

[2] I. Akhatov, O. Lindau, A. Topolnikov, R. Mettin, N. Vakhitova, and W. Lauterborn, Collapse and rebound of a laser-induced cavitation bubble, Phys. Fluids **13**, 2805 (2001).

[3] R. E. A. Arndt, Cavitation in fluid machinery and hydraulic structures, Annu. Rev. Fluid Mech. **13**, 273 (1981).

[4] A. Vogel, W. Lauterborn, and R. Timm, Optical and acoustic investigations of the dynamics of laser-produced cavitation bubbles near a solid boundary, J. Fluid Mech. **206**, 299 (1989).

[5] X. Escaler, E. Egusquiza, M. Farhat, F. Avellan, and M. Coussirat, Detection of cavitation in hydraulic turbines, Mech. Syst. Signal Process. **20**, 983 (2006).

[6] E. Rambod, M. Beizaie, M. Shusser, S. Milo, and M. Gharib, A physical model describing the mechanism for formation of gas microbubbles in patients with mitral mechanical heart valves, Ann. Biomed. Eng. **27**, 774 (1999).

[7] J. K. Jakobsen and R. B. Keller, Jr., Liquid rocket engine turbopump inducers, NASA Report No. NASA-SP-8052, 1971 (unpublished).

[8] S. N. Patek and R. L. Caldwell, Extreme impact and cavitation forces of a biological hammer: Strike forces of the peacock mantis shrimp *Odontodactylus scyllarus*, J. Exp. Biol. **208**, 3655 (2005).

[9] C. E. Brennen, Cavitation in medicine, Interface Focus **5**, 20150022 (2015).

[10] J. E. Field, The physics of liquid impact, shock wave interactions with cavities, and the implications to shock wave lithotripsy, Phys. Med. Biol. **36**, 1475 (1991).

[11] W. Sass, M. Braunlich, H.-P. Dreyer, E. Matura, W. Folberth, H.-G. Priesmeyer, and J. Seifert, The mechanisms of stone disintegration by shock waves, Ultasound Med. Biol. **17**, 239 (1991).

[12] T. Yu, Z. Wang, and T. J. Mason, A review of research into the uses of low level ultrasound in cancer therapy, Ultrasonics Sonochem. **11**, 95 (2004).

[13] W. D. Song, M. H. Hong, B. Lukyanchuk, and T. C. Chong, Laser-induced cavitation bubbles for cleaning of solid surfaces, J. Appl. Phys. **95**, 2952 (2004).

[14] R. Hickling and M. S. Plesset, Collapse and rebound of a spherical bubble in water, Phys. Fluids **7**, 7 (1964).

[15] S. Fujikawa and T. Akamatsu, Effects of the non-equilibrium condensation of vapour on the pressure wave produced by the collapse of a bubble in a liquid, J. Fluid Mech. **97**, 481 (1980).

[16] D. Fuster, C. Dopazo, and G. Hauke, Liquid compressibility effects during the collapse of a single cavitating bubble, J. Acoust. Soc. Am. **129**, 122 (2011).

[17] F. Magaletti, L. Marino, and C. M. Casciola, Shock Wave Formation in the Collapse of a Vapor Nanobubble, Phys. Rev. Lett. **114**, 064501 (2015).

[18] A. Vogel and W. Lauterborn, Acoustic transient generation by laser-produced cavitation bubbles near solid boundaries, J. Acoust. Soc. Am. **84**, 719 (1988).

[19] C.-D. Ohl, T. Kurz, R. Geisler, O. Lindau, and W. Lauterborn, Bubble dynamics, shock waves and sonoluminescence, Philos. Trans. R. Soc. A **357**, 269 (1999).

[20] C.-T. Hsiao, A. Jayaprakash, A. Kapahi, J.-K. Choi, and G. L. Chahine, Modelling of material pitting from cavitation bubble collapse, J. Fluid Mech. **755**, 142 (2014).

[21] L. K. Wang, Z. F. Zhang, and S. P. Wang, Pressure characteristics of bubble collapse near a rigid wall in compressible fluid, Appl. Ocean Res. **59**, 183 (2016).

[22] G. N. Sankin, W. N. Simmons, S. L. Zhu, and P. Zhong, Shock Wave Interaction with Laser-Generated Single Bubbles, Phys. Rev. Lett. **95**, 034501 (2005).

[23] O. Lindau and W. Lauterborn, Cinematographic observation of the collapse and rebound of a laser-produced cavitation bubble near a wall, J. Fluid Mech. **479**, 327 (2003).

[24] O. Supponen, P. Kobel, D. Obreschkow, and M. Farhat, The inner world of a collapsing bubble, Phys. Fluids **27**, 091113 (2015).

[25] W. Lauterborn and A. Vogel, in *Bubble Dynamics and Shock Waves*, edited by C. F. Delale, Shock Wave Science and Technology Reference Library Vol. 8 (Springer, Berlin, 2013), p. 67.

[26] E. Johnsen and T. Colonius, Numerical simulations of non-spherical bubble collapse, J. Fluid Mech. **629**, 231 (2009).

[27] G. L. Chahine, A. Kapahi, J.-K. Choi, and C.-T. Hsiao, Modeling of surface cleaning by cavitation bubble dynamics and collapse, Ultrasonics Sonochem. **29**, 528 (2016).

[28] P. Koukouvinis, M. Gavaises, O. Supponen, and M. Farhat, Simulation of bubble expansion and collapse in the vicinity of a free surface, Phys. Fluids **28**, 052103 (2016).

[29] P. Koukouvinis, M. Gavaises, O. Supponen, and M. Farhat, Numerical simulation of a collapsing bubble subject to gravity, Phys. Fluids **28**, 032110 (2016).

[30] O. Supponen, D. Obreschkow, M. Tinguely, P. Kobel, N. Dorsaz, and M. Farhat, Scaling laws for jets of single cavitation bubbles, J. Fluid Mech. **802**, 263 (2016).

[31] D. Obreschkow, M. Tinguely, N. Dorsaz, P. Kobel, A. de Bosset, and M. Farhat, Universal Scaling Law for Jets of Collapsing Bubbles, Phys. Rev. Lett. **107**, 204501 (2011).

[32] J. R. Blake, The Kelvin impulse: Application to cavitation bubble dynamics, J. Aust. Math. Soc. Ser. B **30**, 127 (1988).

[33] D. Obreschkow, M. Tinguely, N. Dorsaz, P. Kobel, A. de Bosset, and M. Farhat, The quest for the most spherical bubble: Experimental setup and data overview, Exp. Fluids **54**, 1503 (2013).

[34] Y. L. Levkovskii and V. P. Il'in, Effect of surface tension and viscosity on the collapse of a cavitation bubble, Inzh. Fiz. Zh. **14**, 903 (1968).

[35] L. Rayleigh, On the pressure developed in a liquid during the collapse of a spherical cavity, Philos. Mag. **34**, 94 (1917).

[36] P. Gregorčič, R. Petkovšek, and J. Možina, Investigation of a cavitation bubble between a rigid boundary and a free surface, J. Appl. Phys. **102**, 094904 (2007).

[37] A. Vogel, S. Busch, and U. Parlitz, Shock wave emission and cavitation bubble generation by picosecond and nanosecond optical breakdown in water, J. Acoust. Soc. Am. **100**, 148 (1996).

[38] M. Tinguely, D. Obreschkow, P. Kobel, N. Dorsaz, A. de Bosset, and M. Farhat, Energy partition at the collapse of spherical cavitation bubbles, Phys. Rev. E **86**, 046315 (2012).

[39] See Supplemental Material at http://link.aps.org/supplemental/10.1103/PhysRevFluids.2.093601 for movies.

[40] J. B. Keller and M. Miksis, Bubble oscillations of large amplitude, J. Acoust. Soc. Am. **68**, 628 (1980).

[41] B. Ward and D. C. Emmony, Direct observation of the pressure developed in a liquid during cavitation bubble collapse, Appl. Phys. Lett. **59**, 2228 (1991).

[42] J. R. Sukovich, P. A. Anderson, A. Sampathkumar, D. F. Gaitan, Y. A. Pishchalnikov, and R. G. Holt, Outcomes of the collapse of a large bubble in water at high ambient pressures, Phys. Rev. E **95**, 043101 (2017).

[43] D. Obreschkow, M. Bruderer, and M. Farhat, Analytical approximations for the collapse of an empty spherical bubble, Phys. Rev. E **85**, 066303 (2012).

[44] G. L. Chahine, Interaction between an oscillating bubble and a free surface, J. Fluids Eng. **99**, 709 (1977).

[45] J. R. Blake and D. C. Gibson, Growth and collapse of a vapour cavity near a free surface, J. Fluid Mech. **111**, 123 (1981).

[46] J. R. Blake, B. B. Taib, and G. Doherty, Transient cavities near boundaries Part 2. Free surface, J. Fluid Mech. **181**, 197 (1987).

[47] Q. X. Wang, K. S. Yeo, B. C. Khoo, and K. Y. Lam, Nonlinear interaction between gas bubble and free surface, Comput. Fluids **25**, 607 (1996).

[48] P. B. Robinson, J. R. Blake, T. Kodama, A. Shima, and Y. Tomita, Interaction of cavitation bubbles with a free surface, J. Appl. Phys. **89**, 8225 (2001).

[49] A. Pearson, E. Cox, J. R. Blake, and S. R. Otto, Bubble interactions near a free surface, Eng. Anal. Boundary Elements **28**, 295 (2004).

[50] S. Zhang, S. P. Wang, and A. M. Zhang, Experimental study on the interaction between bubble and free surface using a high-voltage spark generator, Phys. Fluids **28**, 032109 (2016).

[51] B. B. Taib, G. Doherty, and J. R. Blake, Proceedings of the Eighth Australasian Fluid Mechanics Conference, 1983 (unpublished).

[52] The code for the numerical simulations is available online at https://obreschkow.shinyapps.io/bubbles [30].

[53] S. Li, R. Han, A. M. Zhang, and Q. X. Wang, Analysis of pressure field generated by a collapsing bubble, Ocean Eng. **117**, 22 (2016).

[54] P. Cui, A. M. Zhang, and S. P. Wang, Small-charge underwater explosion bubble experiments under various boundary conditions, Phys. Fluids **28**, 117103 (2016).

[55] H. Schoeffmann, H. Schmidt-Kloiber, and E. Reichel, Time-resolved investigations of laser-induced shock waves in water by use of polyvinylidenefluoride hydrophones, J. Appl. Phys. **63**, 46 (1988).

[56] A. G. Doukas, A. D. Zweig, J. K. Frisoli, R. Blrngruber, and T. F. Deutsch, Non-invasive determination of shock wave pressure generated by optical breakdown, Appl. Phys. B **53**, 237 (1991).

[57] A fit with the exponent of $\rho c^2 \Delta p$ as a free parameter was also performed, which consistently gave 0.506 ± 0.006.

[58] The presence of the closest surface to the bubble, i.e., the parabolic mirror, is accounted for when determining ζ for bubbles collapsing in microgravity.

[59] J. Holzfuss, M. Rüggeberg, and A. Billo, Shock Wave Emissions of a Sonoluminescing Bubble, Phys. Rev. Lett. **81**, 5434 (1998).